

# Rapid wavefront shaping using an optical gradient acquisition.

Sagi Monin, Marina Alterman, Anat Levin

Department of Electrical and Computer Engineering, Technion, Israel.

## Abstract

Wavefront shaping systems aim to image deep into scattering tissue by reshaping incoming and outgoing light to correct aberrations caused by tissue inhomogeneity. However, the desired modulation depends on the unknown tissue structure and therefore its estimation is a challenging time-consuming task. Most strategies rely on coordinate descent optimization, which sequentially varies each modulation parameter and assesses its impact on the resulting image. We propose a rapid wavefront shaping scheme that transitions from coordinate descent to gradient descent optimization, using the same measurement to update all modulation parameters simultaneously. To achieve this, we have developed an analytical framework that expresses the gradient of the wavefront shaping score with respect to all modulation parameters. Although this gradient depends on the unknown tissue structure, we demonstrate how it can be inferred from the optical system's measurements. Our new framework enables rapid inference of wavefront shaping modulations. Additionally, since the complexity of our algorithm does not scale with the number of modulation parameters, we can achieve very high-resolution modulations, leading to better corrections in thicker tissue layers. We showcase the effectiveness of our framework in correcting aberrations in a coherent confocal microscope.

**Keywords:** wavefront shaping, deep tissue imaging, aberration correction

## 1 Introduction

Optical imaging of tissue is an ongoing challenge because cells and other tissue components scatter light. As a result, as light propagates deeper into tissue, it becomes heavily aberrated, making it impossible to resolve a clear image of deeper structures.

Over the decades, several techniques such as confocal microscopy [1] and optical coherence tomography (OCT) [2] have been developed to achieve deeper imaging by filtering out scattered photons and isolating ballistic photons to form an image. Despite this progress, these techniques are inherently limited to thin layers as the number of ballistic photons decays rapidly within scattering material. To overcome this challenge, wavefront shaping was introduced. Instead of filtering out the scattered photons, wavefront shaping aims to measure the scattered light and invert the process. Such corrections follow two major approaches: digital and optical.

Digital aberration corrections methods attempt to illuminate the tissue using a set of wavefronts and measure the scattered light. This data is fitted to a parametric model explaining the aberration and the hidden target [3–14]. This approach has led to impressive results, but it is ultimately limited by signal-to-noise ratios (SNR). Even with advanced gating strategies, light scattered by deeper tissue components is weak and can be lost in measurement noise.

An alternative class of techniques uses optical wavefront-shaping [15–19]. Such techniques use spatial light modulators (SLMs) in the incoming and/or outgoing paths of the optical system. These SLMs reshape the incoming and/or outgoing wavefront in a way that is the inverse of the aberration it undergoes inside the tissue such that an incoming wavefront can focus into a point despite tissue aberration, and light emerging from a single spot inside the tissue can be reshaped by the SLM and brought into a single sensor point. Unlike digital aberration corrections, the significant advantage of optical wavefront shaping is that the correction is physical, hence all light photons emerging from a single target point can be brought into a single sensor point and measured with a significantly higher SNR.

Wavefront shaping ideas have found applications in a wide range of imaging modalities, including sound [17, 20] and light, coherent imaging and OCT [21], and incoherent fluorescence imaging using single-photon [22–25] and multi-photon [15, 26] excitation. This work showcase a simple aberration correction in a coherent, reflection mode confocal microscope. However, our framework directly applies to other popular imaging schemes such as OCT and fluorescent microscopy.

The practical application of wavefront shaping is hindered by the challenge of determining the wavefront correction to apply. This wavefront correction differs between different tissue layers, and can vary even within different regions of the same tissue sample. Earlier proof-of-concept demonstrations employed a validation camera behind the tissue to provide feedback to the algorithm [27–32]. Another approach use a so-called guide star [17, 21, 26, 33–40], where scattering originates from a strong single point source within the tissue, allowing a wavefront sensor [35, 40] to directly measure the scattered wavefront.

In the absence of such a guide-star, determining a wavefront shaping correction is a significantly more challenging task. Most approaches define a score function to evaluate the quality of the modulation based on the captured signal, and attempt to adjust the SLM parameters until this score is maximized. A core challenge for such optimization algorithms lies in the unknown structure of the tissue. This structure can only be probed by projecting multiple modulation patterns and imaging their scattered output. Thus, most wavefront shaping optimization schemes employ coordinate-descent

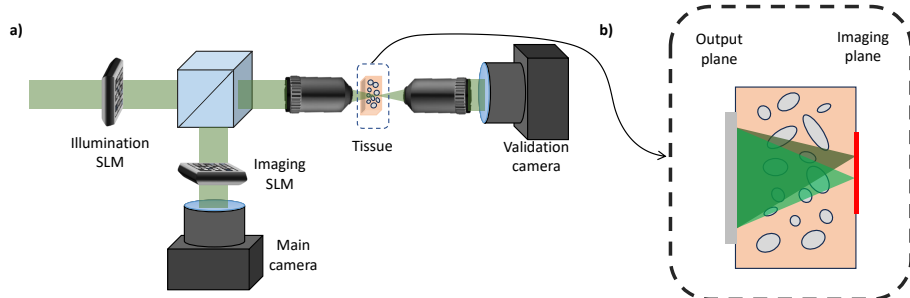


**Fig. 1 System Schematic:**(a) Schematic diagram of our system consisting two SLMs. The first SLM modulates the illuminating laser light, while the second SLM modulates the reflected light. A validation camera provides reference images and confirms focusing on the desired target. (b) Our algorithm optimizes SLM phase to focus light on multiple adjacent points, by applying simple tilt-shift to same modulation.

(CD) approaches, where a single parameter of the modulation is varied at a time. Each optimization step involves selecting a new value for one parameter to improve the modulation score. Such schemes sequentially iterate through all degrees of freedom [22, 24, 26–28, 32, 41]. The main drawback of coordinate descent schemes is their time complexity, which scales with the number of free parameters in the modulation. For thick tissue, the modulation should ideally use all pixels on the SLM, usually in the megabyte range. Some faster wavefront-shaping approaches have been introduced based on iterative time reversal [20, 23, 42–45]. However, these methods are not directly associated with a score function, and therefore there is no principled way to adjust them so that the resulting modulation satisfies various desired properties.

In this research we derive a fast wavefront shaping estimation algorithm capable of simultaneously updating all SLM parameters, and explicitly optimizing a desired score function. Our approach begins by analytically differentiating the wavefront-shaping score. Although the derivative depends on the unknown tissue structure *we propose an innovative imaging scheme that can capture the gradient, with respect to all SLM pixels, in one shot.* Thus, we transition from a coordinate descent schemes to a gradient descent approach and update all SLM parameters at once.

Our gradient descent scheme is significantly faster than existing coordinate descent schemes and can also recover better modulations. Coordinate descent schemes typically restrict the number of SLM modes they optimize due to computational complexity and the high noise sensitivity in measuring high-frequency modes. In thick tissue where the scattering is wide, the optimal modulation requires a large number of degrees of freedom. In contrast, our approach can optimize a large number of modes with no increase in computational complexity. We show that this higher number of modes allow us to find significantly better modulations.

## 2 Results

### 2.1 Background

**Imaging setup:** In Fig. 1 we visualize a wavefront-shaping imaging setup. A laser beam illuminates a tissue sample via a microscope objective. A phase SLM in the illumination arm modulates the illumination pattern. Our goal is to image a target within the tissue layer. Coherent light back-scattered from the target is collected via the same objective, and redirected by a beam-splitter. A second phase SLM in the imaging arm modulates the reflected light. Lastly, the modulated light is measured by the front main camera. The two SLMs in our setup are conjugate to each other. Our setup incorporates a validation camera positioned behind the tissue sample. This camera serves to evaluate focusing quality and capture an undistorted reference image of the target. While earlier research demonstrations of wavefront-shaping utilized this camera to provide feedback to the algorithm, we emphasize that our goal is to develop non-invasive techniques relying solely on feedback by the main (front) camera. It is crucial to note that the validation camera *does not* provide any input to our algorithm.

To maximize the correctable area with a single modulation, the SLM should ideally be placed conjugate to the aberration [46], namely at a plane in the middle of the tissue. For simplicity, in our experimental setup the SLMs are placed in the Fourier plane. To allow correcting a large field of view with the same pattern we apply on the Fourier pattern a tilt and shift operation [47, 48]. However, the two SLMs in our setup are placed such that they are conjugate to each other.

**Image formation model:** We start by presenting a generalized image formation model for a dual SLM system, comprising an illumination SLM and an imaging SLM. Based on this model we infer the specific model of our imaging system.

We denote the reflection matrix of the tissue as  $\mathcal{R}$ . This matrix describes propagation of light from the illumination SLM plane through the tissue and optics, and back to the imaging SLM. That is, for every wavefront  $\mathbf{u}^i$  placed on the illumination SLM, the resulting wavefront before the imaging SLM is modeled as a linear transformation by the reflection matrix:

$$\mathcal{R}\mathbf{u}^i. \tag{1}$$

By placing a modulation  $\mathbf{u}^o$  on the imaging SLM the wavefront reaching the camera is expressed as:

$$\mathcal{P}(\mathbf{u}^o \odot (\mathcal{R}\mathbf{u}^i)). \tag{2}$$

Where  $\mathcal{P}$  denotes a linear mapping between the imaging SLM to the camera sensor that can be calibrated and described by a 2D matrix as it is independent on the tissue sampled.  $\odot$  denotes point-wise multiplication between two vectors.

Our objective is to use a single SLM modulation to image a small area inside the volume rather than a single point. For that we denote the modulation parameters (the phase values of the SLM) as  $\boldsymbol{\rho}^i, \boldsymbol{\rho}^o$ . To direct this modulation to adjacent points within the scattering tissue, we apply tilt and shift to the SLM modulation [47, 48]. We represent the tilt-shifted modulation directed towards volume point  $\ell$  as  $\mathbf{u}^\ell(\boldsymbol{\rho}^i)$ . Similarly,  $\mathbf{u}^\ell(\boldsymbol{\rho}^o)$  denotes a tilt-shifted modulation on the imaging SLM so that it

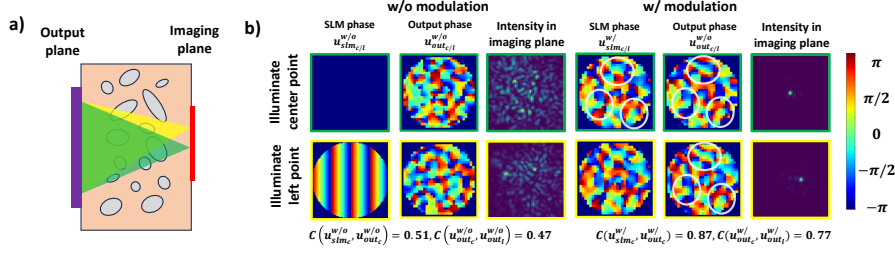


**Fig. 2 Tilt-shift and time reversal effects:**(a) Our algorithm leverages both the memory effect and time-reversal principle to correct for scattered fields. It optimizes for a field where input and output fields are similar and the memory effect is present, ensuring that focusing on adjacent points results in tilt-shifted versions of each other. (b) Simulation results showing the SLM phase, the output phase after tissue reflection, and the intensity on the imaging plane. With light modulation, strong correlations are observed between the SLM phase and output phase  $C(u_{slm_c}^{w/}, u_{out_c}^{w/})$ , as well as between output phases for different points  $C(u_{out_c}^{w/}, u_{out_l}^{w/})$  (correlation scores shown below images; white circles indicate areas of strong correlation). Without aberration correction, correlation decreases rapidly.

collects light from different points in the volume is directed to the same sensor point:

$$\mathcal{P}(u^\ell(\rho^o) \odot (\mathcal{R}u^\ell(\rho^i))). \quad (3)$$

Specifically, the intensity at pixel  $x$  of the camera is:

$$I(x) = |(\zeta_x \odot u^\ell(\rho^o))^T \mathcal{R}u^\ell(\rho^i)|^2, \quad (4)$$

where  $\zeta_x$  is row of the matrix  $\mathcal{P}$  mapping the output of the SLM to a pixel  $x$  on the camera.

In our system,  $\mathcal{R}$  represents the coherent propagation of a monochromatic laser beam. However, in general the same formulation can describe other forms of propagation, such as a path-length resolved reflection matrix describing the measurements of an OCT system. Also  $\mathcal{P}$  can represent various mappings between the imaging SLM plane to the camera sensor plane, depending on an optical setup of choice. In our system, we place the SLM in the Fourier plane hence  $\mathcal{P}$  is a Fourier transformation  $\mathcal{F}$ . **Score function:** We aim to develop an optimization framework that identifies the optimal wavefront modulation for focusing light at a designated plane within scattering tissue. To achieve this, we start by defining a score  $\mathcal{S}(\rho)$  which can quantify a good modulation. We will then attempt to maximize this score to obtain a good modulation:

$$\hat{\rho} = \arg \max_{\rho} \mathcal{S}(\rho). \quad (5)$$

Building upon the work of [24] and recent digital correction approaches [9, 10, 14], we measure the confocal energy of the corrected area. We use the same modulation

$\boldsymbol{\rho}^i = \boldsymbol{\rho}^o$  on both illumination and imaging SLMs, and denote it by a single parameter vector  $\boldsymbol{\rho}$ . We direct and collect light from a point  $\ell$  and measure the intensity at the central sensor pixel. In our system, the mapping between the SLM and camera is Fourier transform. Consequently, the central pixel corresponds to the DC component of the Fourier transform (i.e.  $\boldsymbol{\zeta}_x = \mathbf{1}$ ). Following (4), we can express the measured confocal energy as:

$$I(x) = |\mathbf{u}^\ell(\boldsymbol{\rho})^T \mathcal{R} \mathbf{u}^\ell(\boldsymbol{\rho})|^2. \quad (6)$$

We sum the confocal intensity over an area and measure the total intensity we can collect by a confocal scanning of the modulation, tilted toward different points  $\ell$  in an area of interest  $\mathcal{A}$ :

$$\mathcal{S}(\boldsymbol{\rho}) \equiv \sum_{\ell \in \mathcal{A}} |\mathbf{u}^\ell(\boldsymbol{\rho})^T \mathcal{R} \mathbf{u}^\ell(\boldsymbol{\rho})|^2. \quad (7)$$

We note that in [24] incoherent fluorescence signal was collected and the confocal energy was measured at a single pixel, without attempting to average over an area. Since we use coherent light we notice that if we only direct light to a single spot, a high confocal score at the sensor plane does not guarantee that the light has focused into a single spot inside the tissue, due to various interference effects. To address this, we propose averaging the confocal score over an area, which mitigates these interference effects. This approach aligns with recent coherent digital correction algorithms [9, 10, 14], that optimize over finite isoplanatic patches to maximize the diagonal elements of the reflection matrix which is equivalent to the confocal area score. We investigate the impact of the target area size on focusing performance in our experimental section.

To better illustrate this score, Fig. 2 visualizes the incident and reflected wavefronts, both with and without modulation, for various points within the target area. Initially, without modulation, these wavefronts exhibit minimal correlation. However, once we find a focusing modulation the incoming and outgoing wavefronts demonstrate high correlation. Additionally, we observe a strong memory effect correlation among wavefronts returning from different points.

## 2.2 Optical gradient acquisition

The main challenge in utilizing the score defined in Eq. (7) lies in its dependence on the tissue’s reflection matrix, which is inherently linked to the unknown tissue structure. Since the tissue is treated as a black box, most previous approaches have employed coordinate descent optimization strategies [22, 24, 26–28, 41]. In each iteration, only one parameter is varied (often in a Hadamard basis) and adjusted to improve the measured score. For invasive setups, the score is simply the intensity measured by a validation camera at a point behind the tissue. Given that modern SLMs are in mega-pixel resolution, sequentially scanning each free parameter is an extremely time-consuming process. Consequently, researchers frequently reduce the SLM resolution and correct a significantly smaller number of modes. Below we derive a scheme for measuring the gradient with respect to all SLM parameters in one shot. This approach enables us to transition from coordinate descent schemes to gradient descent scheme, that *update all SLM parameters in each iteration*.

We start by applying the chain rule and differentiate Eq. (7) with respect to the SLM parameters  $\boldsymbol{\rho}$ :

$$\frac{\partial \mathcal{S}(\boldsymbol{\rho})}{\partial \boldsymbol{\rho}} = 2 \sum_{\ell} \underbrace{(\mathbf{u}^{\ell}(\boldsymbol{\rho})^T \mathcal{R} \mathbf{u}^{\ell}(\boldsymbol{\rho}))^*}_{(1)} \cdot \underbrace{(\mathcal{R} \mathbf{u}^{\ell}(\boldsymbol{\rho}) + (\mathbf{u}^{\ell}(\boldsymbol{\rho})^T \mathcal{R})^T)}_{(2)} \odot \underbrace{\frac{\partial \mathbf{u}^{\ell}(\boldsymbol{\rho})}{\partial \boldsymbol{\rho}}}_{(3)}. \quad (8)$$

This gradient is a product of three terms. The first (1) is a complex scalar. The second (2) is a complex vector whose dimensionality is equivalent to that of the modulation. The third term (3), which differentiates the wavefront with respect to the parameters  $\boldsymbol{\rho}$ , can be computed explicitly, and reduces to a simple tilt-shift of the wavefront.

The challenge with the first two terms is that they involve the unknown reflection matrix  $\mathcal{R}$ . Nevertheless, we can leverage the optics to measure the gradient in Eq. (8) for any candidate modulation  $\boldsymbol{\rho}$  of interest. We observe that the complex field  $\mathcal{R} \mathbf{u}^{\ell}(\boldsymbol{\rho})$  is essentially equivalent to applying a modulation at the illumination arm only, and capturing a non-modulated speckle field. The complex field can be captured using a phase retrieval algorithm or with an interferometric imaging system, as detailed in supplementary material. With this measurement, we can numerically compute the remaining terms of Eq. (8). For example, following the reciprocity principle,  $\mathcal{R}$  is a symmetric matrix and  $(\mathbf{u}^{\ell}(\boldsymbol{\rho})^T \mathcal{R})^T$  is equal to  $\mathcal{R} \mathbf{u}^{\ell}(\boldsymbol{\rho})$ . Similarly, the term (1) in Eq. (8) can be computed by multiplying  $\mathcal{R} \mathbf{u}^{\ell}(\boldsymbol{\rho})$  with the known vector  $\mathbf{u}^{\ell}(\boldsymbol{\rho})$ .

By measuring the gradient of the modulation score *we can simultaneously update all entries of the SLM*. This offers a substantial acceleration compared to previous approaches, which iterate through the entries and update only one degree of freedom at a time.

In our current implementation we measured the fields  $\mathcal{R} \mathbf{u}^{\ell}(\boldsymbol{\rho})$  using a phase diversity scheme. This involved applying five defocus wavefronts to the imaging SLM [49, 50], capturing five speckle intensity images, and solving an optimization problem for recovering the phase [51]. We measure each of the  $\ell$  points and sum them. In the supplementary material, we show that the gradient can in fact be imaged directly using a point-diffraction interferometry scheme [52, 53], bypassing the optimization. Moreover, the summation across all points  $\ell$  can be computed within a single exposure, hence the entire gradient can be imaged in one shot.

In supplementary file we also explain that the gradient descent approach derived above resemble fast wavefront shaping algorithms based on time reversal and the power algorithm [20, 23, 42–45]. In fact, it is equivalent to a power iteration of the reflection matrix, if one aims to maximize confocal intensity at a single spot rather than an area. However as we show below a single spot score does not result in good modulations. While power iterations are tied to an eigenvector calculation and may not be adjusted easily to optimize other things, defining a general score function and its gradient provides a more principled way to impose all sort of desired properties on the solution.

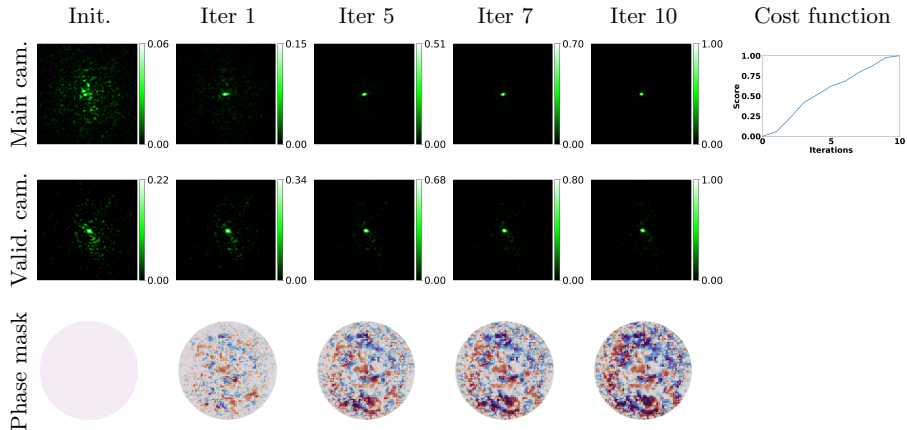


**Fig. 3 Algorithm convergence:** We used our algorithm to image a glass mask partially covered with chrome, placed behind a  $140\mu\text{m}$  thick chicken breast tissue as the scattering material. We show captured images on both the main and validation cameras before the algorithm is applied and at the end of each iteration. The first row demonstrates the algorithm’s convergence over iterations on the main camera for one of the scanned points. The second row displays the convergence on the validation camera, demonstrating our ability to also focus light on the target plane. The final row depicts the evolution of the phase mask presented on both SLMs. The last column illustrates the improvement of the cost function across iterations.

## 2.3 Experimental results

In our experiments we used two types of targets. The first consisted of high-reflectance chrome-coated masks (Nanofilm), patterned using an in-house lithography process to create structures with a resolution of  $2\mu\text{m}$ . We placed these behind scattering layers composed of chicken breast tissue with thickness of  $120\mu\text{m} - 220\mu\text{m}$  or with a number of layers of parafilm. The second target includes polystyrene beads dispersed in agarose gel.

**Imaging:** In Fig. 3 we cover the chrome mask with  $200\mu\text{m}$  thick chicken breast, and demonstrate the algorithm’s efficiency, converging to the desired spot in as few as ten iterations, compared to thousands required by previous coordinate descent algorithms. We show an image of one of the points  $\ell$  in the optimized area  $\mathcal{A}$ , with no modulation and when the optimized modulation is placed on both SLMs. Without modulation we see a noisy speckle image but with the modulation we see a sharp spot whose intensity is about  $20\times$  higher. We also image the chrome mask directly using the validation camera. Without modulation we see a wide speckle pattern, but with modulation on the illumination arm all light propagates through the scattering layer and is focused into a single point on the chrome mask. These validation images ensure that the point we see in the main camera indeed corresponds to a point on the mask, and we are not achieving a point on the main camera by complicated interference effects inside the tissue. At the lower row we show the progress of the phase mask during the iterations.

In Fig. 4, we present imaging results for a few patterns printed on the chrome mask. We display images of a single point in the area through both the main and validation cameras. We also show a confocal scan of the entire area. Without modulation, this



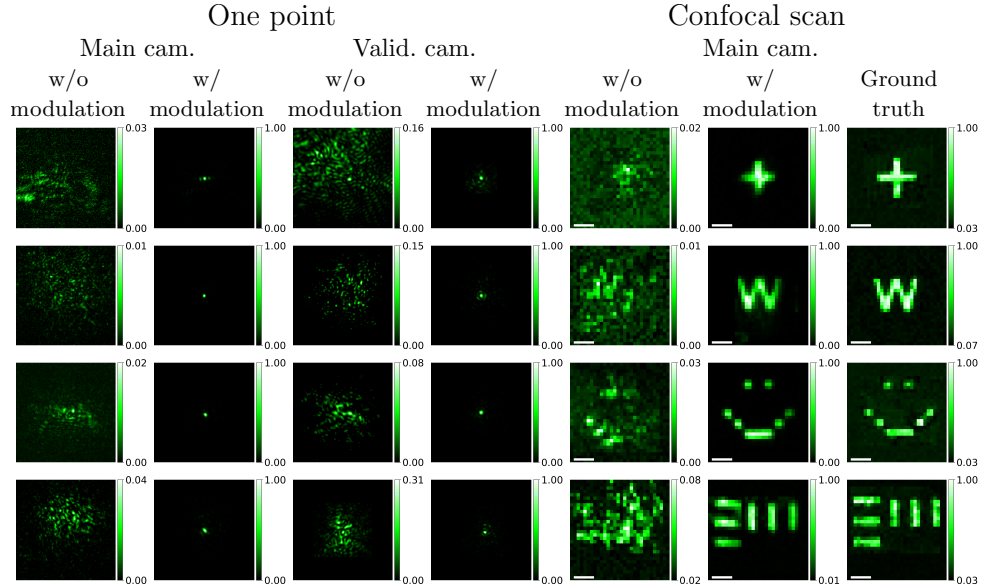


**Fig. 4 Confocal imaging:** of patterns printed on chrome mask, through a scattering layer. Our algorithm successfully focuses light on the desired plane. Each row shows a different target. Columns 1-2: Main camera images of a single focal spot before and after optimization. Columns 3-4: Corresponding validation camera images. Columns 5-7: Confocal scanning results: Without aberration correction, with aberration correction, and reference scan of the target before applying scattering material, respectively. In the first three targets (top rows) the scattering material is chicken breast of thickness of  $120\mu\text{m}$ ,  $150\mu\text{m}$  and  $190\mu\text{m}$ , respectively. In the fourth targets the scattering material is two layers of parafilm. Scale bar on confocal images is  $4\mu\text{m}$ .

looks like a speckle pattern; however, with the modulation, the confocal scan reveals the shape of patterns printed on the chrome mask. Note how the modulation increases light by a factor  $12 - 100\times$ .

**Bead targets:** We demonstrate that our algorithm can also image translucent targets with small variations in refractive indices. In Fig. 5, we present  $3\mu\text{m}$  polystyrene beads dispersed in agarose gel. The slab thickness is  $1.3\text{mm}$  and its optical depth (OD) is 3 (OD is estimated by measuring the attenuation of ballistic light in the validation camera). While a standard confocal scan of such beads is very noisy, with our estimated modulation we can largely increase its contrast and achieve a clear image of spots corresponding to the beads position. To obtain a reference image of the bead positions, we image beads at the further depth of the slab closer to the validation camera, so we are able to image a clear reference from the validation camera. For this reference image, we used a wide-field incoherent illumination.

In the following paragraphs we use again the chrome mask target to evaluate various components of our algorithm.

**Impact of solution resolution:** Our approach is significantly faster than coordinate descent schemes which scan each SLM mode independently. In practice, to reduce scan time coordinate descent schemes optimize for a relatively small number of modes. For

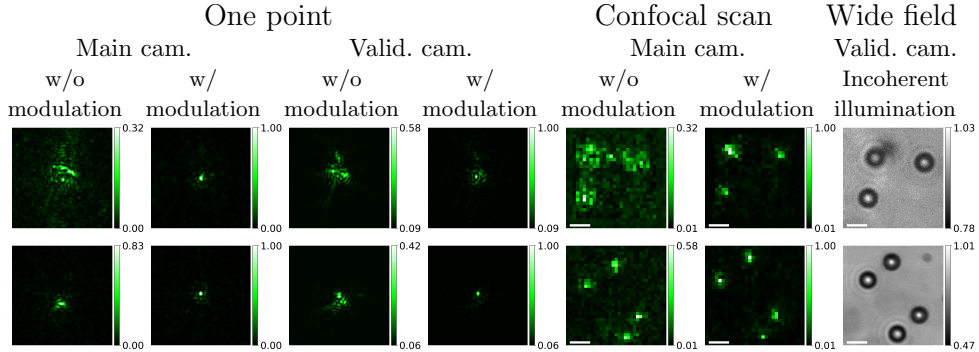


**Fig. 5 Confocal scan of beads:** We show that our algorithm can also be applied on sparser targets. We dispersed  $3\mu\text{m}$  polystyrene beads in agarose gel and image them. Columns 1-2: Main camera images of a single focal spot before and after optimization. Columns 3-4: Corresponding validation camera images. Columns 5-7: Confocal scanning results: Without aberration correction, with aberration correction, and reference image of the target captured by illuminating the sample with incoherent light and capturing with the validation camera.

thick tissue, where the scattering is wide we actually need a large number of modes to obtain a good correction. In Fig. 6, we demonstrate the impact of gradient resolution on our gradient descent algorithm. As shown, higher resolution allows us to focus more energy into a single spot, highlighting the significant influence of resolution on the results

**Comparison with coordinate descent optimization:** Next we explicitly compare our gradient descent scheme with a coordinate descent approach. Following [24, 29], we express the modulation as  $\rho = \sum \phi_k H_k$  where  $H_k$  are elements in an Hadamard basis. We scan the basis elements, adjusting the phase of one basis element at a time. We argue that the resolution of coordinate descent schemes is not only limited by acquisition time, but also by SNR. For high frequency modes, varying  $\phi_k$  results in a very small change to the score, potentially lower than the noise level. In Fig. 7 we show that the coordinate descent score cannot improve beyond a certain point. To illustrate that noise is the limiting factor, we run another coordinate descent scheme, but this time we averaged multiple shots for each basis element to reduce noise. This oversampling approach allowed us to update the high frequency modes, leading to much better results. However, the oversampling is also  $5\times$  slower than the standard coordinate descent scheme and  $125\times$  slower than our gradient descent scheme. The modulation computed in Fig. 7 is a low-resolution one. For higher resolution modulations the time difference between coordinate descent and gradient descent approaches would be even larger.

**Impact of scanned area:** In Fig. 8, we evaluate the effect of the area  $\mathcal{A}$  over which the score is optimized. If this area is small we observe a sharp spot at the main camera but the light did not actually focus into a spot inside the tissue as it does not correspond to a spot at the validation camera, indicating that the spot at the main camera results from interference of coherent light within the tissue. This issue does not occur with fluorescent wavefront shaping [24] since the incoherent emissions from

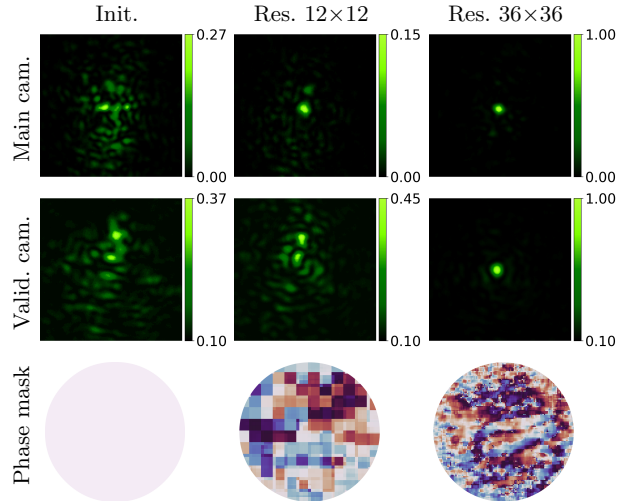


**Fig. 6 Impact of phase mask resolution:** We evaluate the effectiveness of gradient descent (GD) solutions using phase masks of varying resolutions. We place the chrome mask behind two layers of parafilm, creating a significant aberration. Results demonstrate that higher-resolution phase masks yield superior solutions, enabling convergence in both the main and validation cameras.

nearby fluorescent points do not interfere. As we increase the size of the scanned area, requiring the same modulation to explain multiple points, such interference effects disappear, and we achieve a point in both cameras. However, as we increase the target area the intensity of the focused spot at the main camera decays because the correction required by nearby points vary spatially and one modulation cannot explain a wide area. This is due to the fact that memory effect correlation does not hold for very large ranges.

The challenge in computing a wavefront shaping modulation is that the desired modulation depends on the unknown tissue structure. As a result, most previous optimization strategies are based on slow coordinate descent strategies, which sequentially scan the parameters of the modulation and quarry them one at a time. Our contribution is in finding an analytic way to compute the gradient of the wavefront shaping score from the scattered wavefront, and we can compute the gradient in closed-form, despite the fact that we do not know the tissue structure. With this analytic expression we can move from coordinate descent into gradient descent optimization and update all SLM parameters at once. The resulting optimization strategy is orders of magnitude faster and allow us to estimate high resolution modulations. Such high resolution modulations allow us to get better corrections.

We demonstrated the applicability of our gradient acquisition framework using a simple confocal-microscope setup. To make better usage of wavefront shaping corrections in real tissue imaging applications, our framework can be incorporated into an OCT or fluorescent microscopes systems. OCT enables imaging insider deep tissue volumes as it isolates content at different depths using path-length filtering. However,

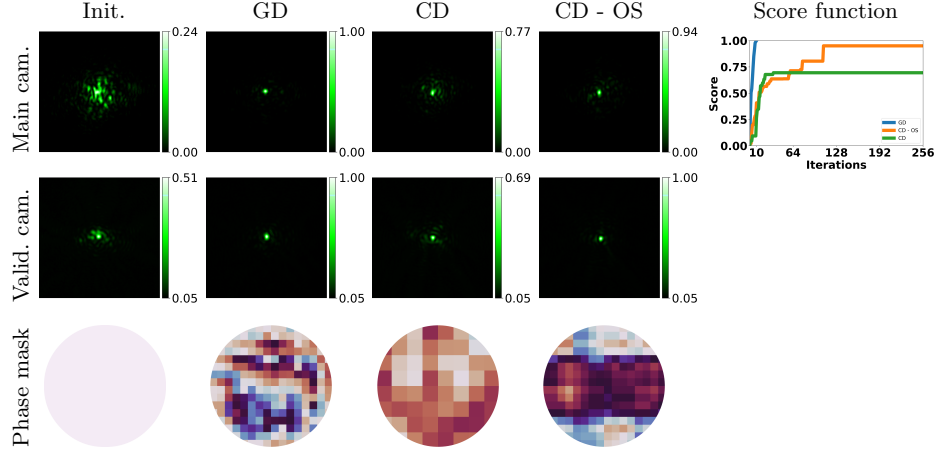


**Fig. 7 Comparison of gradient descent and coordinate descent schemes:** We compare our gradient descent (GD) optimization to coordinate descent (CD) using the Hadamard basis. Due to CD's time-intensive nature, we optimize for a low-resolution mask and used a weak aberration volume (a single layer of parafilm tape). To address CD's susceptibility to noisy measurements, we test two configurations: Standard CD where to estimate the phase of each basis element using 5 shots. This approach could not improve the score behind a certain point, because the improvement in the score is lower than the imaging noise. We next used an over-sampled CD (CD-OS) capturing twenty-four images per basis element. This over-sampled version is less susceptible to noise and reached a higher confocal score, at the cost of an even longer acquisition. Overall, our results demonstrate that GD converges significantly faster than both CD variants and exhibits greater robustness to noise.

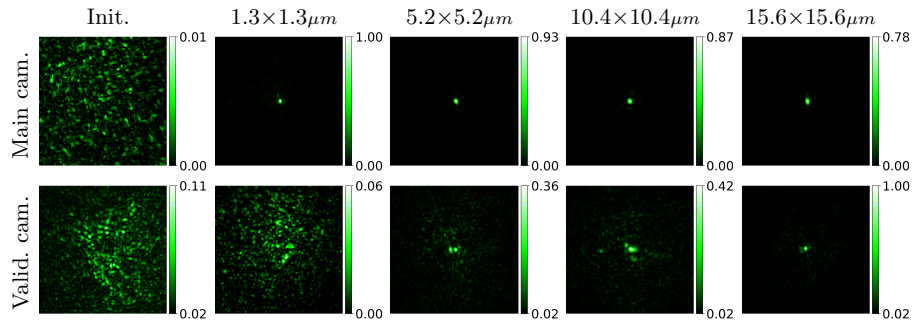


**Fig. 8 Effect of target area size:** We evaluate how focusing quality depends of the size of the target area  $\mathcal{A}$  over which the confocal score is computed. The experiment used a chrome-covered glass mask overlaid with  $140\mu\text{m}$  thick chicken breast tissue. Our results show that for single-spot illumination (second column) the algorithm successfully achieved a sharp focused spot on the main camera without actually focusing light to a spot inside the tissue, as evident by the image from the validation camera. As we expanded the size of the focus area, the algorithm demonstrated progressively improved ability to focus light inside the tissue and the validation camera images are sharper. At the same time increasing the scanned area reduces the intensity of the focused spot on the main camera because a single modulation cannot correct very large areas.

for deep tissue OCT filtering is also subject to severe aberrations which can be corrected with a wavefront shaping system. The optimization framework presented in this paper applies directly to an OCT system as well, and can be used to develop a fast, aberration corrected OCT. Wavefront shaping is also highly effective in correcting the aberrations of a fluorescent microscope. We can use a very small modification of the algorithm to handle incoherent light. However, because the number of photons emitted from a fluorescent target is very low, measuring the gradient with sufficient SNR may be challenging.

Our rapid gradient-descent optimization algorithm resembles fast time-reversal algorithms [20, 23, 42–45] for wavefront shaping, which use the power iteration method to estimate the eigenvectors of the reflection matrix. We discuss the relationship between these algorithms in supplementary file. We show that if one indeed aims at estimating the eigenvectors of the reflection matrix, the gradient derived above is fully equivalent to a power iteration. However, for coherent imaging the largest eigenvector of the reflection matrix is not always a good modulation and adjustment to the power iteration methods often use ad-hoc approaches. Defining a target score and its gradient provides a more principled way to navigate the modulation search into a desired result.

### 3 Methods

**System design:** Our setup is fully depicted in the supplementary Fig. ?? . A collimated laser beam (CPS532 Thorlabs) illuminates a phase SLM (GAEA 2 Holoeye). The light is then focused with objective lens (N20X-PF Nikon) on the target plane through the scattering material. The reflected light from the target is collected through the same objective-lens is modulated by a second SLM (LETO Holoeye). Finally the light is imaged with a camera (Atlas-314S Lucid vision labs). The second SLM (LETO Holoeye) has two functions: create phase pattern used for estimating the out going wavefront via a phase-retrieval algorithm. The second use is to place the conjugate of the retrieved phase in order to show confocal scanned images and calculate the score function. In our setup the SLMs are placed in the Fourier plane of the target. Additional details on the setup, calibration and alignment can be found in the supplementary material.

**Experimental targets:** For our targets we use high-reflecting chrome-coated chrome mask (Nanofilm) and use in-house lithography process to create pattern with resur-rection of  $2\mu m$ . For scattering material we used chicken breast tissue with thickness of  $120\mu m - 220\mu m$  or with a number of layers of parafilm, as started in the text. For all targets chrome-mask results except for the results in Fig. 8 the target area for the algorithm was  $\mathcal{A} = 15.6\mu m \times 15.6\mu m$  and the sampling interval was  $1.3\mu m$  matching the focus spot size of the objective lens. After the algorithm convergence the final confocal scan was done with sampling interval of  $0.65\mu m$ . For the target on the fourth row of Fig. 4 the target spans over an area larger than  $\mathcal{A} = 15.6\mu m \times 15.6\mu m$ . Hence, we run the algorithm four times in partially overlapping areas and stitch the results together to form the final image. For the bead targets in Fig. 5, since the beads

are sparser the target area was  $\mathcal{A} = 20.75\mu m \times 20.75\mu m$ . The sampling interval was  $0.65\mu m$  for both algorithm and final confocal scan.

## References

- [1] Elliott, A.D.: Confocal microscopy: Principles and modern practices. *Current Protocols in Cytometry* **92**(1), 68 (2020)
- [2] Jr, A., Harris, A., Gross, J., Januleviciene, I., Shah, A., Siesky, B.: Optical coherence tomography angiography: An overview of the technology and an assessment of applications for clinical research. *British Journal of Ophthalmology* **101** (2016)
- [3] Choi, W., Fang-Yen, C., Badizadegan, K., Oh, S., Lue, N., Dasari, R.R., Feld, M.S.: Tomographic phase microscopy. *Nature methods* **4**(9), 717–719 (2007) <https://doi.org/10.1038/nmeth1078>
- [4] Choi, Y., Yang, T.D., Fang-Yen, C., Kang, P., Lee, K.J., Dasari, R.R., Feld, M.S., Choi, W.: Overcoming the diffraction limit using multiple light scattering in a highly disordered medium. *Phys. Rev. Lett.* (2011)
- [5] Kang, S., Jeong, S., Choi, W., Ko, H., Yang, T.D., Joo, J.H., Lee, J.-S., Lim, Y.-S., Park, Q.-H., Choi, W.: Imaging deep within a scattering medium using collective accumulation of single-scattered waves. *Nature Photonics* **9**(4), 253–258 (2015) <https://doi.org/10.1038/nphoton.2015.24>
- [6] Badon, A., Barolle, V., Irsch, K., Boccara, A.C., Fink, M., Aubry, A.: Distortion matrix concept for deep optical imaging in scattering media. *Science Advances* (2020)
- [7] Kwon, Y., Hong, J.H., Yoon, S., Kang, S., Lee, H., Jo, Y., Kim, K.H., Choi, W.: Computational conjugate adaptive optics for longitudinal through-skull imaging of cortical myelin. *bioRxiv* (2022)
- [8] Kang, S., Kwon, Y., Lee, H., Kim, S., Hong, J., Yoon, S., Choi, W.: Tracing multiple scattering trajectories for deep optical imaging in scattering media. *Nature communications* **14**(1) (2023)
- [9] Zhang, Y., Dinh, M., Wang, Z., Zhang, T., Chen, T., Hsu, C.W.: Deep imaging inside scattering media through virtual spatiotemporal wavefront shaping. *arXiv preprint arXiv:2306.08793* (2024)
- [10] Lee, Y., Kim, D., Jo, Y., Kim, M., Choi, W.: Exploiting volumetric wave correlation for enhanced depth imaging in scattering medium. *Nature communications* **14**(1) (2023)
- [11] Feng, B.Y., Guo, H., Xie, M., Boominathan, V., Sharma, M.K., Veeraraghavan,

- A., Metzler, C.A.: Neuws: Neural wavefront shaping for guidestar-free imaging through static and dynamic scattering media. *Science Advances* **9**(26), 4671 (2023)
- [12] Yeminy, T., Katz, O.: Guidestar-free image-guided wavefront shaping. *Science Advances* **7**(21), 5364 (2021)
- [13] Haim, O., Boger-Lombard, J., Katz, O.: Image-guided computational holographic wavefront shaping. *Nature Photonics* (2024)
- [14] Balondrade, P., Barolle, V., Guigui, N., Auriant, E., Rougier, N., Boccara, C., Fink, M., Aubry, A.: Multi-spectral reflection matrix for ultrafast 3d label-free microscopy. *Nature Photonics* **18**(10), 1097–1104 (2024)
- [15] Ji, N.: Adaptive optical fluorescence microscopy. *Nature Methods* **14**, 374–380 (2017)
- [16] Hampson, K., Turcotte, R., Miller, D., Kurokawa, K., Males, J., Ji, N., Booth, M.: Adaptive optics for high-resolution imaging. *Nature Reviews Methods Primers* **1**, 68 (2021)
- [17] Horstmeyer, R., Ruan, H., Yang, C.: Guidestar-assisted wavefront-shaping methods for focusing light into biological tissue. *Nature Photonics* **9**(9), 563–571 (2015) <https://doi.org/10.1038/nphoton.2015.140>
- [18] Yu, H., Park, J., Lee, K., Yoon, J., Kim, K., Lee, S., Park, Y.: Recent advances in wavefront shaping techniques for biomedical applications. *Current Applied Physics* **15**(5), 632–641 (2015)
- [19] Gigan, S., Katz, O., *et al.*: Roadmap on wavefront shaping and deep imaging in complex media. *Journal of Physics: Photonics* **4**(4), 042501 (2022) <https://doi.org/10.1088/2515-7647/ac76f9>
- [20] Prada, C., Thomas, J.-L., Fink, M.: The iterative time reversal process: Analysis of the convergence. *The Journal of the Acoustical Society of America* **97**(1), 62–71 (1995) <https://doi.org/10.1121/1.412285>
- [21] Jang, J., Lim, J., Yu, H., Choi, H., Ha, J., Park, J.-H., Oh, W.-Y., Jang, W., Lee, S., Park, Y.: Complex wavefront shaping for optimal depth-selective focusing in optical coherence tomography. *Opt. Express* **21**(3), 2890–2902 (2013) <https://doi.org/10.1364/OE.21.002890>
- [22] Boniface, A., Blochet, B., Dong, J., Gigan, S.: Noninvasive light focusing in scattering media using speckle variance optimization. *Optica* **6**(11), 1381–1385 (2019) <https://doi.org/10.1364/optica.6.001381>

- [23] Aizik, D., Gkioulekas, I., Levin, A.: Fluorescent wavefront shaping using incoherent iterative phase conjugation. *Optica* **9**(7), 746–754 (2022)
- [24] Aizik, D., Levin, A.: Non-invasive and noise-robust light focusing using confocal wavefront shaping. *Nature communications* **15**(5575) (2024)
- [25] Stern, G., Katz, O.: Noninvasive focusing through scattering layers using speckle correlations. *Optics Letters* **44**(1), 143 (2018) <https://doi.org/10.1364/ol.44.000143>
- [26] Katz, O., Small, E., Guan, Y., Silberberg, Y.: Noninvasive nonlinear focusing and imaging through strongly scattering turbid layers. *Optica* **1**(3), 170–174 (2014)
- [27] Vellekoop, I.M., Mosk, A.P.: Focusing coherent light through opaque strongly scattering media. *Opt. Lett.* **32**(16), 2309–2311 (2007) <https://doi.org/10.1364/OL.32.002309>
- [28] Conkey, D.B., Brown, A.N., Caravaca-Aguirre, A.M., Piestun, R.: Genetic algorithm optimization for focusing through turbid media in noisy environments. *Optics Express* **20**(5), 4840 (2012) <https://doi.org/10.1364/oe.20.004840>
- [29] Popoff, S.M., Lerosey, G., Carminati, R., Fink, M., Boccarda, A.C., Gigan, S.: Measuring the transmission matrix in optics: An approach to the study and control of light propagation in disordered media. *Physical Review Letters* **104**(10), 100601 (2010) <https://doi.org/10.1103/physrevlett.104.100601>
- [30] Vellekoop, I.M., Lagendijk, A., Mosk, A.P.: Exploiting disorder for perfect focusing. *Nature Photonics* **4**(5), 320–322 (2010) <https://doi.org/10.1038/nphoton.2010.3>
- [31] Yaqoob, Z., Psaltis, D., Feld, M.S., Yang, C.: Optical phase conjugation for turbidity suppression in biological samples. *Nature Photonics* **2**(2), 110–115 (2008) <https://doi.org/10.1038/nphoton.2007.297>
- [32] Chen, Y., Sharma, M.K., Sabharwal, A., Veeraraghavan, A., Sankaranarayanan, A.C.: 3PointTM: Faster measurement of high-dimensional transmission matrices. In: *Euro. Conf. Computer Vision (ECCV)* (2020)
- [33] Tang, J., Germain, R.N., Cui, M.: Superpenetration optical microscopy by iterative multiphoton adaptive compensation technique. *Proceedings of the National Academy of Sciences* **109**(22), 8434–8439 (2012) <https://doi.org/10.1073/pnas.1119590109>
- [34] Wang, C., Liu, R., Milkie, D.E., Sun, W., Tan, Z., Kerlin, A., Chen, T.-W., Kim, D.S., Ji, N.: Multiplexed aberration measurement for deep tissue imaging in vivo. *Nature Methods* **11**(10), 1037–1040 (2014) <https://doi.org/10.1038/nmeth.3068>



- [35] Liu, T.L., Upadhyayula, S., Milkie, D.E., Singh, V., Wang, K., Swinburne, I.A., Mosaliganti, K.R., Collins, Z.M., Hiscock, T.W., Shea, J., Kohrman, A.Q., Medwig, T.N., Dambournet, D., Forster, R., Cunniff, B., Ruan, Y., Yashiro, H., Scholpp, S., Meyerowitz, E.M., Hockemeyer, D., Drubin, D.G., Martin, B.L., Matus, D.Q., Koyama, M., Megason, S.G., Kirchhausen, T., Betzig, E.: Observing the cell in its native state: Imaging subcellular dynamics in multicellular organisms. *Science* **360**(6386), 1392 (2018) <https://doi.org/10.1126/science.aaq1392>
- [36] Fiolka, R., Si, K., Cui, M.: Complex wavefront corrections for deep tissue focusing using low coherence backscattered light. *Opt. Express* **20**(15), 16532–16543 (2012)
- [37] Xu, X., Liu, H., Wang, L.V.: Time-reversed ultrasonically encoded optical focusing into scattering media. *Nature Photonics* **5**, 154–157 (2011)
- [38] Wang, Y.M., Judkewitz, B., DiMarzio, C.A., Yang, C.: Deep-tissue focal fluorescence imaging with digitally time-reversed ultrasound-encoded light. *Nature Communications* **3**(1), 928 (2012) <https://doi.org/10.1038/ncomms1925>
- [39] Kong, F., Silverman, R.H., Liu, L., Chitnis, P.V., Lee, K.K., Chen, Y.C.: Photoacoustic-guided convergence of light through optically diffusive media. *Opt. Lett.* **36**(11), 2053–2055 (2011)
- [40] Vellekoop, I.M., Cui, M., Yang, C.: Digital optical phase conjugation of fluorescence in turbid tissue. *Applied Physics Letters* **101**(8), 081108 (2012) <https://doi.org/10.1063/1.4745775>
- [41] Popoff, S.M., Aubry, A., Lerosey, G., Fink, M., Boccara, A.C., Gigan, S.: Exploiting the time-reversal operator for adaptive optics, selective focusing, and scattering pattern analysis. *Phys. Rev. Lett.* **107**, 263901 (2011) <https://doi.org/10.1103/PhysRevLett.107.263901>
- [42] Song, H.C., Kuperman, W.A., Hodgkiss, W.S., Akal, T., Ferla, C.: Iterative time reversal in the ocean. *The Journal of the Acoustical Society of America* **105**(6), 3176–3184 (1999) <https://doi.org/10.1121/1.424648>
- [43] Ruan, H., Jang, M., Judkewitz, B., Yang, C.: Iterative time-reversed ultrasonically encoded light focusing in backscattering mode. *Scientific reports* **4**, 7156 (2014) <https://doi.org/10.1038/srep07156>
- [44] Si, K., Fiolka, R., Cui, M.: Breaking the spatial resolution barrier via iterative sound-light interaction in deep tissue microscopy. *Scientific reports* **2**, 748 (2012) <https://doi.org/10.1038/srep00748>
- [45] Papadopoulos, I., Jouhannau, J.-S., Poulet, J., Judkewitz, B.: Scattering compensation by focus scanning holographic aberration probing (f-sharp). *Nature*

Photonics (2016)

- [46] Mertz, J., Paudel, H., Bifano, T.G.: Field of view advantage of conjugate adaptive optics in microscopy applications. *Applied Optics* (2015)
- [47] Alterman, M., Bar, C., Gkioulekas, I., Levin, A.: Imaging with local speckle intensity correlations: theory and practice. *ACM TOG* (2021)
- [48] Osnabrugge, G., Horstmeyer, R., Papadopoulos, I.N., Judkewitz, B., Vellekoop, I.M.: Generalized optical memory effect. *Optica* **4**(8), 886–892 (2017) <https://doi.org/10.1364/optica.4.000886>
- [49] Dean, B.H., Bowers, C.W.: Diversity selection for phase-diverse phase retrieval. *J. Opt. Soc. Am. A* **20**(8), 1490–1504 (2003) <https://doi.org/10.1364/JOSAA.20.001490>
- [50] Gonsalves, R.A.: Phase Retrieval And Diversity In Adaptive Optics. *Optical Engineering* **21**(5), 215829 (1982) <https://doi.org/10.1117/12.7972989>
- [51] Candes, E.J., Li, X., Soltanolkotabi, M.: Phase retrieval via wirtinger flow: Theory and algorithms. *IEEE Transactions on Information Theory* **61**(4), 1985–2007 (2015)
- [52] Smartt, R.N., Steel, W.H.: Theory and application of point-diffraction interferometers. *Japanese Journal of Applied Physics* **14**(S1), 351 (1975) <https://doi.org/10.7567/JJAPS.14S1.351>
- [53] Akondi, V., Jewel, A., Vohnsen, B.: Digital phase-shifting point diffraction interferometer. *Optics Letters* **39**, 1641–4 (2014) <https://doi.org/10.1364/OL.39.001641>

# Rapid wavefront shaping using an optical gradient acquisition- supplementary material.

Sagi Monin, Marina Alterman, Anat Levin

Department of Electrical and Computer Engineering, Technion, Israel.

## 1 Optical system

**System:** A drawing of our system is shown in Fig. 1. A laser is collimated and passes through a polarizer to align the laser polarization with the SLM main-axis. The wavefront is then modulated by the illumination-SLM and reflected towards the sample. The modulated light passes through an objective lens and illuminates the sample. The forward scattering light continues to the validation camera which is used for validating focus of our algorithm on the image plane. The reflected light from the sample returns through the same objective lens and is splitted at a beam-splitter towards the imaging-SLM which again modulates the wavefront. Finally the light is collected by the main-camera sensor. The imaging-SLM has two functions: The first is to present the optimized pattern  $\mathbf{u}^\ell(\boldsymbol{\rho})$  when measuring the score function and when confocal scanning a target. The second function is to present different defocus phase functions for capturing patterns for phase diversity optimization.

A full component list of our system: 532nm laser (CPS532 Thorlabs), P - linear polarizer (LPNIRB100 Thorlabs), L1 - 100mm achromatic lens, L2 - 400mm achromatic lens, L3 - 150mm achromatic lens, L4 - 100mm achromatic lens, L5 - 200mm achromatic lens, TL - tube lens (TTL200-A Thorlabs), BS - beamsplitter (62-882 Edmund), OL1 - objective lens NA=0.5, MAG= $\times 20$  (N20X-PF Nikon), OL2 - objective lens NA=0.7, MAG= $\times 100$  (MY100X-806 Mitutoyo). Lens translation stage is a single-axis stage (PT1 Thorlabs) with a motorized actuator (Z925B Thorlabs). The sampler holder was custom created with three translation stages (PT1 Thorlabs) allowing adjust the target in all three-axes. For the main camera we use A314S Atlas (Lucid vision) and for the validation camera we use Grasshopper3 USB3 (Teledyne Flir).

### Alignment and calibration:

We start by explaining how we align our system. To modulate the Fourier transform of the wave the illumination-SLM needs to be at the focal plane of the lens after it

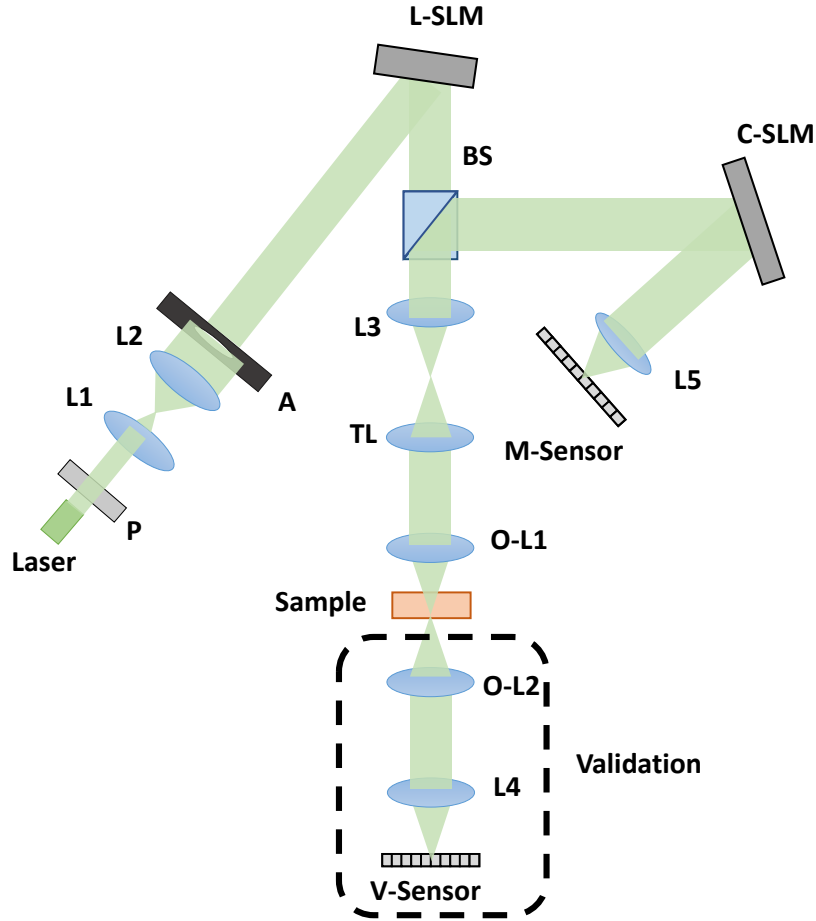


**Fig. 1 Setup:** we present the full setup of optical system. Light starting the from the laser is reflected from the laser-SLM towards the sample. The reflected light from the sample returns through the same path where it relected from the camera-SLM and is then collected by the main-sensor. The transmitted light from the sample continues to the validation sensor which is only used to validate our results. C-L: collimation lens, P:polarizer, M:mirror, L-SLM: laser-SLM, BS:beam-splitter, L-lens, O-L:objective lens, V-sensor:Validation sensor, C-SLM: camera sensor M-Sensor:Main sensor.

(L3 in Fig. 1), and the imaging-SLM at the focal plane of the lens before it (same L3). We perform this alignment by using a third camera focused at infinity (we place an appropriate laser line filter ( $532nm$ ) ad focus the camera at a far building). Then place two polarizers: before the SLM at degree of  $45^\circ$  and after the SLM at degree of  $135^\circ$ . Putting the polarizers in these angles will result in a dark pixel of the SLM pixel doesn't modulate the light and on a white pixel if it modulates by  $\pi$ . We then focus on the SLM through the relevant lens, forming a rely system. We display a checkerboard

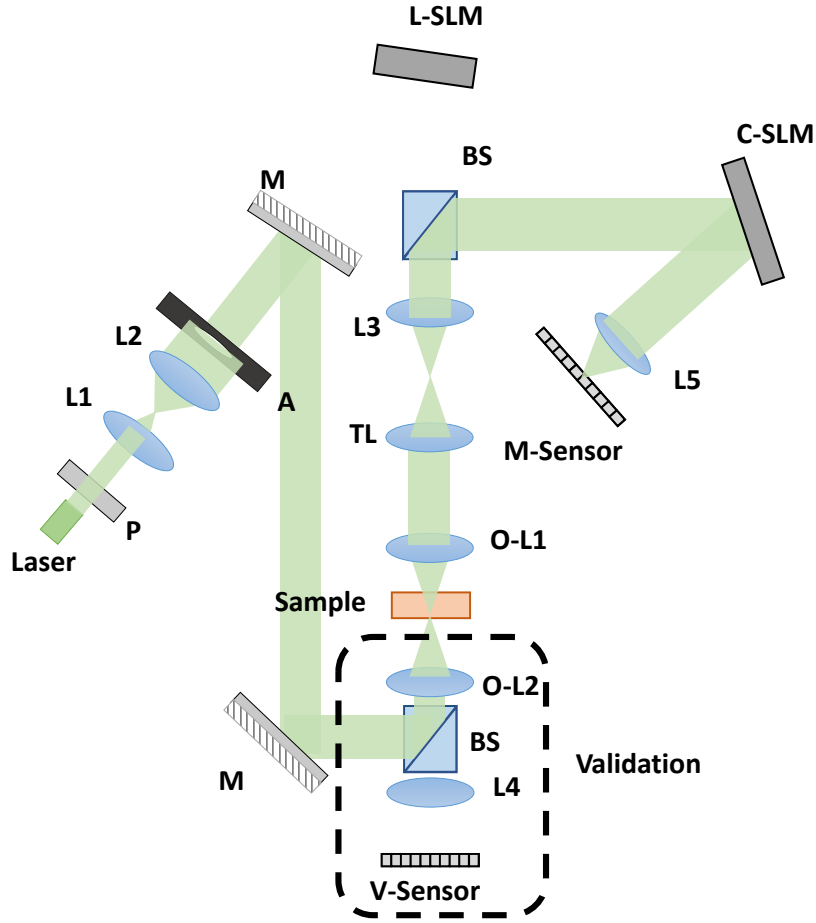


**Fig. 2 Back calibration:** We use a back-path laser to calibrate our system, here we show that laser path using back-path.

pattern on the SLM and adjust the distance between the SLM and the lens until we get a sharp image. We also calibrate the distance between the main/validation cameras and the lenses before them (L4/L5) to ensure they are focused at infinity.

After the system is aligned, we find the relevant area on both SLMs which are illuminated and pass through the objective lens aperture. The relevant area size can be calculated based on size of the aperture and pixel size. We describe how we calibrate the illumination-SLM and the imaging-SLM follows a similar procedure. In order to find the center  $(x_c, y_c)$  we use the following procedure: We start by placing a mirror on in the sample holder and move the sample holder until we achieve focus at the main-camera. To get an initial estimate of the centers we present a sinusoidal pattern

of the same size of the aperture on the SLM and move it on  $x - y$  axes of the SLM and look when we get a maximum intensity at the target pixel (if we do not modulate the right area on the SLM less light is directed to that target pixel), this gives us a initial estimate of  $(x_e, y_e)$ . We then place a defocus pattern (quadratic phase  $((x - (x_c - x_e))^2 + (y - (y_c - y_e))^2)$ ) on the laser SLM and move the sample holder until again we achieve focus on the main-camera. Ideally if  $(x_c, y_c) = (x_0, y_0)$  the location of the laser spot will be at the same  $x - y$  location no matter what quadratic phase we introduce. If the location of the laser spot is different we modify our estimation. We repeat this until the focus doesn't change. This is then repeated for the imaging-SLM while the illumination-SLM presents blank phase.

Next, we calibrate the mapping between the SLMs and the main camera. Using the focal length of the lens before the camera (L5), the SLM pitch and the wavelength of the emitted light, we can map between SLM frequencies to the camera pixel using simple geometry. However, this mapping doesn't account for misalignment in rotation of the SLMs. To overcome this we fine-tune the calibration by displaying sinusoidal patterns and recording the shift presented on the main camera. Using these measurements we estimate the rotation of the SLM.

Finally, we find the mapping between the two SLMs. To do this we follow a similar procedure as in [1, 2], where instead of a using a florescent bead we illuminate the target from the back bypassing the L-SLM i.e. we place mirrors so the laser is directed through O-L2 and after the sample the light continues to main camera, as shown in Fig. 2. We then recover the modulation pattern by applying phase-diversity optimization. The Helmholtz reciprocity (phase conjugation) principle [3] dictates that if we place the conjugate of the recovered wavefront the illumination-SLM, it will focus into a point behind the scattering tissue. Hence, we redirect the laser to the forward path (i.e. through the illumination-SLM and O-L1) and place the modulation pattern on illumination-SLM and we expect to achieve a focused point on the validation camera. However, if the mapping between the SLMs is wrong we don't get a focused point on the validation camera. Now we can find the mapping between the SLMs by shifting the pattern on the illumination-SLM until the energy on the focused point on the validation camera is maximum.

As our score maximizes the confocal intensity over an area we rely on the tilt shift memory effect. To apply the scan we need to recover the parameter determining the ratio between the tilt and shift. To determine this parameter we again follow a similar calibration method as [1, 2]; however, since they rely on florescent beads we again illuminate the target by illuminating the target from the back bypassing the L-SLM. We then recover the modulation pattern by applying phase-diversity optimization. We then redirect the laser to the forward path (i.e. through the illumination-SLM and O-L1) and place the modulation pattern on illumination-SLM and we use the validation camera to view the focused spot. We then adjust the ratio between tilt and shift of the modulation pattern so that we can move the focused spot in the validation camera, while preserving maximal intensity.

**Gradient step:** When performing gradient descent optimization we need to choose a step-size at each iteration. In our system, we use backtracking line search [4]. For each iteration we start with a predefined step size and after the step we measure the

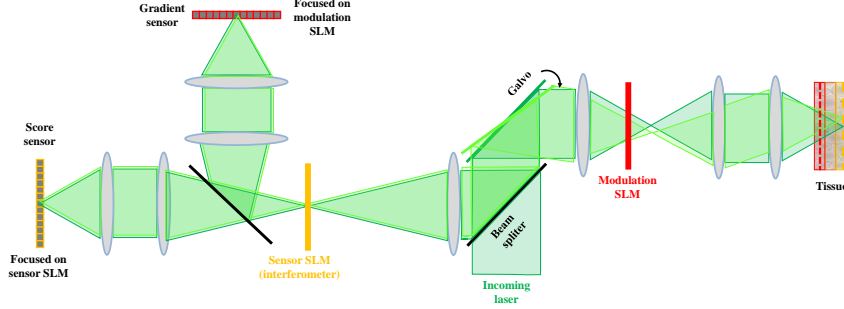


**Fig. 3 Setup for interferometric gradient acquisition:** An incoming laser beam is directed to focus on a point inside the tissue, the focal point can be shifted with a galvo. The figure illustrates two such tilted paths in two shades of green. On its way to the sample the beam passes through a relay system, containing an SLM for aberration correction. The SLM is placed such that it is conjugate to a plane inside the tissue volume. Another SLM is used as an interferometer to modulate the reflected light captured by the sensor. Two cameras are used in this setup - the first is focused on the interferometer SLM and termed score sensor. The second sensor is focused on the modulation SLM and termed gradient sensor.

score function. If the score function increases we perform the step; however, if the score decreases we do not perform the step. Instead we divide the step size by two and again measure the score. We repeat this until the score increases or until the step size is smaller than some threshold. If the score does not increase we perform a large step (with the initial step size) as the optimization might be stuck in a local-maximum. At the end of optimization we choose the phase modulation pattern that scored the highest score.

## 2 Gradient acquisition

### 2.1 Gradient acquisition using phase diversity optimization

To acquire the gradient of our wavefront shaping score, we need to capture the complex wavefront emerging at the sensor  $\mathbf{v}^\ell = \mathcal{R}\mathbf{u}^\ell(\boldsymbol{\rho})$ , for every point  $\ell$  in the scanned area  $\mathcal{A}$ . In our current implementation, we do this using a phase diversity optimization scheme [5, 6], for each of the target points. That is, we sequentially placed the wavefronts  $\mathbf{u}^\ell(\boldsymbol{\rho})$  on the illumination SLM and capture the resulting speckle intensity images at the sensor. We place on the camera SLM 5 known defocus wavefronts  $\mathbf{u}_{defocus}^j$  and capture 5 speckle intensity images  $I_\ell^1, \dots, I_\ell^5$ . We use these images to solve an optimization problem retrieving the phase of the complex wavefront from the measured intensity images [7], resulting in the optimization problem:

$$\hat{\mathbf{v}}^\ell = \arg \max_{\mathbf{v}^\ell} \sum_{j=1}^5 \left\| I_\ell^j - |\mathcal{F}(\mathbf{v}^\ell \odot \mathbf{u}_{defocus}^j)|^2 \right\|^2 \quad (1)$$

We scan multiple points  $\ell \in \mathcal{A}$  and repeat the same phase optimization. These wavefronts are averaged to compute one instance of the gradient.

$$\mathcal{R}\mathbf{u}^\ell(\boldsymbol{\rho}) = \mathbf{v}_{estimate}^\ell = \frac{1}{|\mathcal{A}|} \sum_{\ell \in \mathcal{A}} \mathbf{v}^\ell \quad (2)$$

## 2.2 Fast gradient acquisition using point diffraction interferometry

We describe a second future approach for gradient acquisition which would allow us to acquire it much faster, using a small number of only 3 shots. This possible setup would utilize a variant of a point diffraction interferometry system [8, 9], that can capture the complex wavefront with no optimization, and can also average over all  $\ell \in \mathcal{A}$  within one shot.

**Setup for point diffraction interferometry:** Fig. 3 illustrates a setup for gradient acquisition with point diffraction interferometry. A laser beam illuminates a tissue sample, and an SLM can modulate its shape. The SLM is placed such that it is conjugate to a plane inside the tissue, where the aberration is actually happening. The illumination wavefront propagates through the scattering tissue, reflects from its internal structure and back-scatters to the camera. The returning light passes through the same SLM on its way to the camera. The returning modulated light splits at a beam splitter toward two sensors. Before the sensors, the light passes through another relay system and a second SLM. This second SLM is placed such that it is conjugate to the target we wish to image rather than conjugate to the aberration plane. We refer to the first SLM (closer to the sample) as “the modulation SLM” and to the second one as “the sensor SLM”. After the the sensor SLM the light splits through another beam-splitter toward two sensors. The first sensor (which can also be a single point detector) is place such that it is conjugate to the target points we wish to image and to the sensor SLM, and would measure the confocal intensity score at the center of the frame. The second 2D sensor is placed such that it is conjugate to the modulation SLM and would measure the gradient directly. We refer to these two sensors as the *score sensor*, and the *gradient sensor*.

The setup also includes a galvo that can tilt the incoming and outgoing light. While we can implement such a tilt with the SLM itself, a galvo can be tilted faster than the refresh rate of the SLM. By tilting the incoming beam we can direct it toward different target points  $\ell \in \mathcal{A}$ . Tilting the returning beam implies that the light scattered from target point  $\ell$  is directed to the central pixel of the sensor, regardless of the actual spatial position of  $\ell$ . In this setup, to modulate the scene with the wavefront  $\mathbf{u}^\ell(\boldsymbol{\rho})$ , we place  $\boldsymbol{\rho}$  on the SLM and use the galvo to tilt it toward the target point  $\ell$ , so effectively we get:

$$\mathbf{u}^\ell(\boldsymbol{\rho})(x) = \boldsymbol{\zeta}_x \odot e^{\frac{2\pi i}{\lambda}(\tau^\ell \cdot x)} \odot \boldsymbol{\rho}(x) \quad (3)$$

where  $\tau^\ell$  represents the tilt toward point  $\ell$ .  $\boldsymbol{\zeta}_x$  represents here the shape of the illumination wavefront reaching the modulation SLM. Since our SLM is not placed at the Fourier plane of the system, it is illuminated by a spherical wavefront and not by a plane wave. Note that  $\boldsymbol{\zeta}_x$  was defined in the main paper as the (known) propagation of



the wavefront from the modulation SLM to the center of the sensor, since we assume our system is fully symmetric the same  $\zeta_x$  applies both on the incoming and on the outgoing paths.

**Interferometric measurements:** We start with a mathematical expression for the wavefront we will measure by the gradient sensor. We recall that this sensor is focused at the modulation SLM and directly images the wavefront at this plane. If we use a flat phase on the sensor SLM, and display the modulation  $\mathbf{u}^\ell(\boldsymbol{\rho})$  (by displaying  $\boldsymbol{\rho}$  on the modulation SLM and combining it with the proper galvo tilt), it will measure the 2D wavefront

$$\mathbf{v}^\ell = (\mathbf{u}^\ell(\boldsymbol{\rho})) \odot (\mathcal{R}\mathbf{u}^\ell(\boldsymbol{\rho})) \quad (4)$$

where  $\mathcal{R}\mathbf{u}^\ell(\boldsymbol{\rho})$  is the propagation of the incoming modulated illumination via the tissue and back to the SLM plane. On the SLM plane, each coordinate is multiplied again by  $\mathbf{u}^\ell(\boldsymbol{\rho})$ . We use the notation  $\odot$  to denote an element-wise multiplication between two 2D fields. Since we image the modulation SLM plane we measure this as a 2D wavefront and not as a scalar.

Next, denote by  $\mu^\ell$  the complex scalar reaching the center of the score sensor. As this sensor is focused on the target plane (and on the sensor SLM, which is conjugate to the target plane):

$$\mu^\ell = (\mathbf{u}^\ell(\boldsymbol{\rho}))^T \mathcal{R}\mathbf{u}^\ell(\boldsymbol{\rho}) \quad (5)$$

If we could place an aperture on pixel  $x$  of the 2nd sensor SLM, the 2D wavefront we measure at the gradient sensor (which is focused on the modulation SLM) is governed by the scalar  $\mu^\ell$  and corresponds to

$$\mathbf{v}_1^\ell = \mu^\ell \cdot \zeta_x^* \quad (6)$$

Where  $\zeta_x$ , defined in Eq. (2) of the main paper encodes the (known) propagation from the modulation SLM plane to the center of the score sensor. We denote the difference between the wavefronts in Eqs. (4) and (6) by

$$\mathbf{v}_2^\ell = \mathbf{v}^\ell - \mathbf{v}_1^\ell. \quad (7)$$

Moreover, rather than using a pinhole on the sensor SLM, we suggest to vary the phase of pixel  $x$  of the sensor SLM to  $\phi_j$  while keeping all other pixels at phase 0. This implies that the gradient sensor would see the wavefront  $\mathbf{v}_2^\ell + e^{i\phi_j}\mathbf{v}_1^\ell$ . We can use standard phase shifting interferometry and measure  $J = 3$  intensity images while varying the phase  $\phi_j$  of the central pixel equally between 0 and  $2\pi$ . We measure

$$I_j^\ell = |\mathbf{v}_2^\ell + e^{i\phi_j}\mathbf{v}_1^\ell|^2 = e^{-i\phi_j}\mathbf{v}_1^{\ell*}\mathbf{v}_2^\ell + e^{i\phi_j}\mathbf{v}_1^\ell\mathbf{v}_2^{\ell*} + |\mathbf{v}_1^\ell|^2 + |\mathbf{v}_2^\ell|^2. \quad (8)$$

By summing the intensity images with the corresponding phase we can isolate the interference term

$$\mathbf{v}_1^{\ell*}\mathbf{v}_2^\ell = \sum_j e^{i\phi_j} I_j^\ell \quad (9)$$

We can also measure  $|\mathbf{v}_1^\ell|^2$  and add it to Eq. (9) to receive

$$g^\ell = \mathbf{v}_1^{\ell*}\mathbf{v}^\ell \quad (10)$$

We can now substitute Eqs. (3), (4) and (6), and check the content of this interference term:

$$g^\ell = \mu^{\ell*} \cdot (\zeta_x \odot \mathbf{u}^\ell(\boldsymbol{\rho})) \odot (\mathcal{R}\mathbf{u}^\ell(\boldsymbol{\rho})) \quad (11)$$

$$= \underbrace{\mu^{\ell*}}_{(1)} \cdot \underbrace{\zeta_x \odot \boldsymbol{\rho}}_{(2)} \odot \underbrace{\zeta_x \odot e^{\frac{2\pi i}{\lambda}(\tau^\ell \cdot x)}}_{(3)} \odot \underbrace{(\mathcal{R}\mathbf{u}^\ell(\boldsymbol{\rho}))}_{(4)} \quad (12)$$

Comparing this formula to the gradient derived in Eq. (5) of the main paper, we see that it corresponds to the desired gradient up to known multiplicative terms. Term (1) corresponds to term (1) of the gradient, term (2) is a known multiplicative factor, term (3) is effectively the derivative of the tilted modulation  $\mathbf{u}^\ell(\boldsymbol{\rho})$  with respect to the SLM parameters  $\frac{\partial \mathbf{u}^\ell(\boldsymbol{\rho})}{\partial \boldsymbol{\rho}}$ , which is term (3) in Eq. (5) of the main paper, see definition in Eq. (3). Term (4) is equivalent to term (2) in Eq. (5) of the main paper.

Moreover, note that to average over target point  $\ell \in \mathcal{A}$  all we need to do is to scan the galvo toward a different direction, without changing the pattern  $\boldsymbol{\rho}$  on the SLM. This effectively implies that we can tilt the galvo *within exposure*, and capture 3 speckle images

$$I_j = \sum_{\ell} I_j^\ell \quad (13)$$

From these 3 images we can compute the gradient directly.

The above derivation suggest a possible future implementation of our wavefront shaping algorithm, that will allow us to image the gradient of the confocal score directly, using as little as 3 shots, where the scanning over the target area is done within exposure. Furthermore since we use an interferometer no phase diversity optimization is required and the complex wavefront is measured directly.

**Equivalence to power iterations:** The gradient derived above is similar to rapid time reversal based approach for wavefront shaping. These approach start from the assumption that the desired modulation is the largest eigenvector of the reflection (or transmission) matrix of the tissue. This eigenvector can be estimated very efficiently using power iterations. In each iteration, one displays a modulation  $\mathbf{u}$  on the SLM, measures  $\mathcal{R}\mathbf{u}$  and use it as the next guess for the modulation. The gradient we derived above collapse to such power iteration where the target area  $\mathcal{A}$  consists of a single point (no summation over multiple  $\ell$  values). However, as demonstrated in Fig. XX of the main paper, given a coherent target averaging over an area is crucial for getting a good wavefront correction. Without this interference can bring all light into a strong point at the sensor, without actually focusing the light into a single point inside the volume. Attempting to adjust power algorithms to produce different modulations may require ad-hoc additions. However defining a target score and deriving its gradient provides a more principle framework to impose desired properties on the modulation.

The point diffraction interferometry setup suggested above is particularly similar to the incoherent phase conjugation algorithm of [2]. To prove the convergence of the incoherent power iterations the supplementary file of [2] assumes that the phase of the captured wavefront is captured precisely with a point diffraction interferometer. This phase estimation is equivalent to the gradient derived above.

## References

- [1] Aizik, D., Levin, A.: Non-invasive and noise-robust light focusing using confocal wavefront shaping. *Nature communications* **15**(5575) (2024)
- [2] Aizik, D., Gkioulekas, I., Levin, A.: Fluorescent wavefront shaping using incoherent iterative phase conjugation. *Optica* **9**(7), 746–754 (2022)
- [3] Mugnier, L.M., Blanc, A., Idier, J.: Phase diversity: A technique for wavefront sensing and for diffraction-limited imaging. *Advances in Imaging and Electron Physics*, vol. 141, pp. 1–76. Elsevier (2006). [https://doi.org/10.1016/S1076-5670\(05\)41001-0](https://doi.org/10.1016/S1076-5670(05)41001-0)
- [4] Armijo, L.: Minimization of functions having Lipschitz continuous first partial derivatives. *Pacific Journal of Mathematics* **16**(1), 1–3 (1966)
- [5] Dean, B.H., Bowers, C.W.: Diversity selection for phase-diverse phase retrieval. *J. Opt. Soc. Am. A* **20**(8), 1490–1504 (2003) <https://doi.org/10.1364/JOSAA.20.001490>
- [6] Gonsalves, R.A.: Phase Retrieval And Diversity In Adaptive Optics. *Optical Engineering* **21**(5), 215829 (1982) <https://doi.org/10.1117/12.7972989>
- [7] Candes, E.J., Li, X., Soltanolkotabi, M.: Phase retrieval via wirtinger flow: Theory and algorithms. *IEEE Transactions on Information Theory* **61**(4), 1985–2007 (2015)
- [8] Smartt, R.N., Steel, W.H.: Theory and application of point-diffraction interferometers. *Japanese Journal of Applied Physics* **14**(S1), 351 (1975) <https://doi.org/10.7567/JJAPS.14S1.351>
- [9] Akondi, V., Jewel, A., Vohnsen, B.: Digital phase-shifting point diffraction interferometer. *Optics Letters* **39**, 1641–4 (2014) <https://doi.org/10.1364/OL.39.001641>